DNA–Gold Nanoparticle Reversible Networks Grown on Cell Surface Marker Sites: Application in Diagnostics

Kyuwan Lee,[†] Vladimir P. Drachev,[‡] and Joseph Irudayaraj[†,*]

[†]Department of Agricultural and Biological Engineering and [‡]School of Electrical and Computer Engineering, Bindley Bioscience Center and Birck Nanotechnology Center, 225 South University Street, Purdue University, West Lafayette, Indiana 47906, United States

ABSTRACT Effective identification of breast cancer stem cells (CSC) benefits from a multiplexed approach to detect cell surface markers that can distinguish this subpopulation, which can invade and proliferate at sites of metastasis. We present a new approach for dual-mode sensing based on targeting using pointer and signal enhancement using enhancer particle networks for detection by surface plasmon resonance (SPR) and surface-enhanced Raman scattering (SERS). We demonstrate our concept to detect cell surface markers, CD44 and CD24, in three breast cancer cell lines to identify a $CD44^+/CD24^-$ subpopulation of CSCs. The designed network structure can be well-controlled and has improved sensitivity compared to conventional approaches with ability to detect a single target on the membrane of a living cell. We have also developed a fractal approach to model the dimension of the network structure and developed an empirical relationship to estimate the number of particles in the network and its size. The empirical equation was validated with experiments and finite-difference time-domain simulations, and the cell phenotyping results were found to be in good agreement with published data from conventional sorting by flow cytometry.

KEYWORDS: network structures · dual-mode SERS and SPR detection · surface plasmon coupling · cancer stem cells · predictive empirical models · fractal dimension

Identification of cancer stem cell surface markers for immunophenotyping has great value in predicting the invasiveness and metastatic potential of tumors.[1] It was established recently with cytometry that a subpopulation of breast cancer cells expressing the CD44 antigen and not the CD24 antigen ($CD44^+/CD24^-$) exhibits enhanced invasive properties typical of stem cells.[2] These two surface markers have been used to characterize three breast cancer cell lines, MCF-7, MDA-MB-231, and MDA-MB-468, with a new cell phenotyping approach developed in this work. Cell phenotyping is usually accomplished by monitoring fluorescence emitted from organic fluorophores[3,4] or quantum dots (Qdot),[5,6] surface plasmon resonance scattering (SPR) of gold nanoparticles,[7–9] or enhanced scattering from Raman spectroscopy.[10–12]

Among the latest technologies, hyperspectral SPR imaging and SERS mapping using gold nanosensors has several advantages, including ease of sample preparation to detect single cells. Further, the use of gold nanoparticles excludes issues of photobleaching and cytotoxicity and enables *in vivo* detection. As shown in this work, the use of gold nanoparticle assemblies has the potential to be highly sensitive; however, the aggregation has to be well-controlled for multiplex detection.

In the past, gold nanospheres or gold nanorods with different aspect ratio have been utilized to detect multiple markers of cancer cells by measuring SPR peaks in scattering mode.[8,13] The limitation of using single nanoparticle probes is the nonspecific binding or aggregation of nanoprobes and their orientation which could result in undefined SPR peaks. Another constraint of single particle sensing is the nanoparticle uptake by cells. In addition, single particle probes on cell membranes have a low signal-to-noise ratio because of the background scattering from cellular organelles. Limitations of network structure approach are the time taken in formation and ability to fabricate multiplex DNA–antibody functionalized nanoparticles.

It is known that nanoparticle aggregates coated with polymers,[14–16] biomolecules,[17,18] and silica[19–21] can serve as excellent candidates as signal enhancers. Small aggregates of gold nanoparticles have the potential to detect single molecules based on SERS[22,23] due to their strong local field enhancement in relation to particle size. The tunability of enhancement based on particle aggregates that results in networks is an attractive feature on which to capitalize for sensitive biomedical

* Address correspondence to josephi@purdue.edu.

Received for review November 13, 2010 and accepted February 2, 2011.

Published online February 11, 2011
10.1021/nn1030862

spectroscopy. However, formation of aggregates with reproducible SPR peak positions and SERS enhancement is still an issue especially under conditions of living cells, when nanoparticles are exposed to physiological conditions for a long period of time during network formation.[24]

Gold nanoparticle networks formed by DNA hybridization have attracted significant interest because of their versatile characteristics.[25−27] Network structures formed due to DNA hybridization of gold nanoparticles can be tuned to form networks of specific size for a given interparticle distance to generate a strong SERS signal[28] and Rayleigh scattering.[29] The quasi-periodic gold nanostructures formed due to DNA hybridization tend to generate a homogeneous local field enhancement in the gaps due to controlled distances between neighboring nanoparticles.[30,31] Consequently, such structures give rise to a well-defined enhancement by SERS[32,33] that we capitalize upon.

In this work, a systematic investigation of the resonance peak control in small aggregates (<150 nm) was accomplished. A DNA-assembled nanoparticle network structure, formed on specific cell surface sites with excellent interparticle distance control, was demonstrated. DNA hybridization and dehybridization on a membrane of living cells shows reversibility of the formed structures. By allowing nanoparticle network formation in real-time, we show that endocytosis can be avoided for network structures of size 120 nm or greater.[34] Finally, we demonstrate feasibility of the DNA−gold nanoparticle probes in dual-mode sensing (SERS and SPR) for multiplex detection of cell surface markers for single cell phenotyping. The expressions of cell surface markers, CD24 and CD44, were determined in three breast cancer cell lines and validated with flow cytometry data.

We first demonstrate a dynamic SERS platform using pointer and enhancer particles for forming and assembling gold nanoparticle networks on single cell surfaces *via* DNA hybridization. Detection of Raman labels in the network by SERS was possible even at a laser power of 1 mW (*e.g.*, 785 nm source) in real-time. Next, we demonstrate the reversibility of the network structure by a simple temperature step and show its disassembly. The cross-platform utility of the network structures, formed by hybridization of ssDNA-functionalized gold nanoparticles, was illustrated by examining its plasmon properties by hyperspectral SPR imaging to complement the SERS mode of detection.

Our design consists of pointer particles to target a cell surface marker and enhancer particles functionalized with ssDNA and Raman labels that aggregate around a pointer particle to form a network structure that can be probed by SERS and hyperspectral SPR. Pointer particles were modified, respectively, with antibodies specific to antigen CD24 (or CD44) and ssDNA of user-defined length. The length of ssDNA of

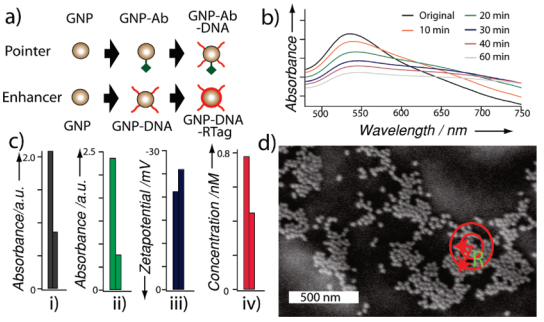

Figure 1. (a) Pointer and enhancer particle synthesis. Enhancer particles are one set of two different complementary particles, although only one is shown. The other enhancer particle is synthesized in exactly the same manner but with different lengths of DNA. (b) UV−vis spectra of reversible DNA−gold nanoparticle hybridization process. (c) Absorbance peak of DNA at 262 nm (i), Raman label (4-mercaptopyridine) at 323 nm in solution (ii) before (left) and after (right) modification. Zeta-potential (iii) of gold nanoparticle before and after modification. Nanoparticle concentration (iv) of the original and final solutions. (d) FESEM image of the DNA hybridized nanoparticle network structure on the MDA-MB-231 cell surface at 5 min of the hybridization time in the 450 pM solution (*R* is the radius of gyration) using pointer and enhancer particles.

the pointers was kept different in the probes designed to detect CD24 and CD44. The enhancer particles were decorated with Raman labels, 4-mercaptopyridine or 4,6-dimethyl-2-pyrimidinethiol, to correspond with CD44 or CD24 markers and complementary ssDNA. Important point to note is that the length of ssDNA used in the pointer and enhancer particles to detect the two marks was kept different so that the rate and time of network formation are different. Thus respective nanoparticle network structures can be formed by DNA hybridization when the two types are mixed. The network structure will thus grow at the membrane marker site targeted by the pointer particle bearing the respective antibody due to antibody−antigen interaction. Nonspecific attachment of the pointer particle to the membrane surface is also possible. However, only enhancer network structures grown on pointer particles will remain on the cell surface after washing steps.

The pointer and enhancer particles were first characterized in solution for hybridization and dehybridization conditions using UV−vis spectroscopy (Figure 1a, b). The signal level in Figure 1c (i) and (ii), respectively, denotes DNA concentration and Raman label concentration of the original solution and the centrifuged supernatant after nanoparticle modification to estimate the numbers of DNA strands and Raman label molecules. Figure 1c (iii) and (iv) denotes the zeta-potential and nanoparticle concentration before and after synthesis. Details of gold nanoparticle (40 nm) synthesis and modification are provided in the Supporting Information (section SI.4). The morphologies of particle assembly and their network structures were first examined by field emission scanning electron microscopy (FESEM). Typically, particle networks can

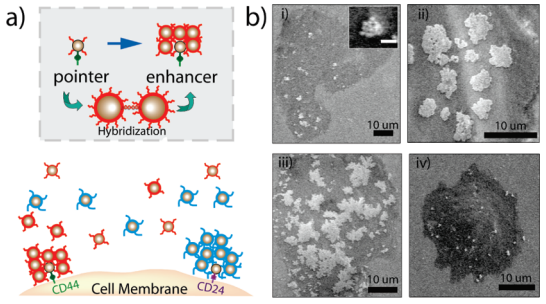

Figure 2. (a) Schematic of the cell marker detection strategy. After targeting a cell surface receptor by a pointer particle, network forming nanoparticles are added to form the network structure. (b) Back scattering SEM images show the growth of network structures due to DNA hybridization with time for MDA-MB-231. The temperature-dependent nature of network formation and its reversibility is illustrated. Each image shows the network structure after a hybridization time of (i) 5 min (inset: 3 min, scale bar = 100 nm), (ii) 20 min, (iii) 40 min, and (iv) after a temperature step above the hybridization melting point (45 °C).

be characterized as a fractal cluster with a fractal dimension characterizing the 3D space. The FESEM image in Figure 1d shows that the nanoparticle network structure that formed at a temperature much lower than the melting point has a fractal dimension of about 1.87 (described in Supporting Information, section SI.1). The fractal dimension for the synthesized structure was estimated for a certain enhancer particle concentration and about 5 min of aggregation time (details are discussed in the Supporting Information). Similar conditions were used for the structures shown in Figure 4 (implying similar fractal dimension) for SPR mapping. Scanning electron microscope images shown in Figure 2b illustrate the formation of aggregates due to change in the network structure with time and dehybridization after heating and explained below. These structural changes correspond to changes in the dimension of the network structure.

Figure 2a shows the schematic of the detection concept to target cell surface receptors using the network structure. First, pointer particles functionalized with either anti-CD44 or anti-CD24 and ssDNA were synthesized with different lengths and bases. Subsequently, two types of enhancer particles with respective Raman labels and complementary ssDNA were synthesized to selectively hybridize with the pointer particles and with each other. Figure 2b (i–iii) shows the dynamic gold nanoparticle network formation at different time periods (5, 20, and 40 min, respectively) after incubating with MDA-MB-231 cells targeting the CD44 cell surface marker. On the basis of the growth model calculations (eq 1), the size of the nanostructure was estimated to be 163 nm after 3 min, yielding a SERS signal in proportion to its size (discussed in Figure 3a,c). Our calculations show a close agreement with the experimental measurement of ~150 nm from the SEM image (Figure 2b, (i) inset). After 5 min, the size of the structure reached ~500 nm, as shown in

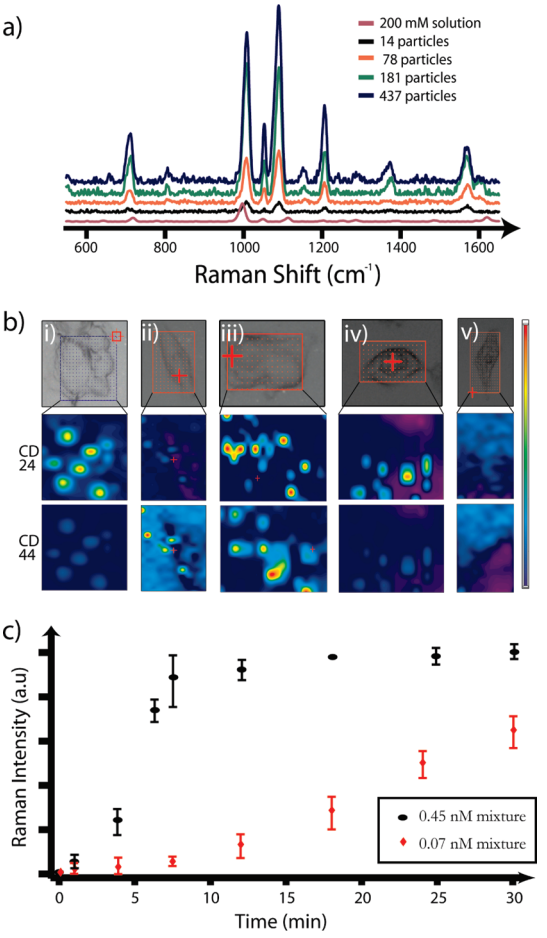

Figure 3. (a) Raman signal intensity increased with respect to network structure formation and the corresponding spectra of Raman tag. (b) Multiplex Raman mapping of CD44/CD24 marker profile from three different cell lines: (i) MCF-7, (ii) MDA-MB-231, and (iii) MDA-MB-468. Optical image of cell lines (top). Mapping of Raman dye 4,6-dimethyl-2-pyrimidinethiol with the characteristic peak at 569 cm^{-1} (middle) and 4-mercaptopyridine with the characteristic peak at 1094 cm^{-1} (bottom) corresponding to CD24 and CD44 markers and its distribution on the cell surface. (iv,v) Temperature-dependent mapping of network formation due to hybridization, presenting clear evidence of the reversibility of gold nanoparticle structure formation (scale bar = minimum 0, maximum 150 photon counts). (c) Raman intensity increase with time for the two different enhancer particle concentrations examined (CD44 detection on MDA-MB-231 cells).

Figure 2b (ii). Results indicated that the size of the network structure was proportional to the SERS intensity (Figure 3c). Hence structures formed within 0 and 3 min could be characterized based on their SERS intensity using our approach. All SERS measurements were performed at a very low laser power using a long-wavelength excitation laser (1 mW, 785 nm) and relatively short acquisition time (3~30 s) to cause minimum damage to cells.

The disassembly of the network structure was demonstrated by raising the temperature of the sample to 45 °C using a control stage (TMS 600, Linkam Scientific Instruments Ltd., UK). The FESEM image in

Figure 2b (iv) confirms the disassembly of the nanoparticle in the network structure. In experiments using living cells, the remaining pointer particles directly bound to the cell surface markers will naturally follow the endocytosis and exocytosis pathways.[34] Eventually, some of the particles could be excreted by the cells, and the viable cells might ultimately retain a minimum number of nanoparticles.[34,35] In our experiments, nanoparticles of size 40−60 nm were used as pointer particles because surface modification is easy and the particle uptake and removal are known.[34] The reversibility is attractive especially for single cell studies since the same cell can be used for further analysis (for example genotyping) once its phenotype is determined. Reversibility of the network structure is discussed further below and in the Supporting Information section SI.7. Comparing the size of nanoparticles to that of the focal area of the microscope (∼1 μm), the structures formed show excellent multiplexing ability when probed by SPR scattering for single cell analysis using nanoparticles with the concentration of ∼450 pM.

An increase in Raman intensity, corresponding to the formation of nanoparticle network structure, was monitored in real-time by measuring the SERS intensity using pointer particles targeting the CD44 marker on MDA-MB-231 cells and subsequently enhanced by the network structure configuration using enhancer particles bearing complementary ssDNA. A distinct increase in Raman intensity was observed as the number of particles in the structure increased (Figure 3a). Raman intensity reached a maximum when nanoparticles fully filled the focal area (∼1 μm in diameter). The number of nanoparticles can thus be calculated as a function of time using the fractal dimension property of the network structure with[36]

$$N(t) = 2^{(t/\tau)} \quad (1)$$

where $\tau = t_0 \times \log 2/\log N_{max}$ and N_{max} = [diameter of focal area/$(D + s)$]^{d_f}. Here, N denotes the number of particles in the focal area, t the time, τ the growth time, t_0 the time taken to reach $N(t_0) = N_{max}$ (N_{max} the number of particles when the nanoparticles fully fill the focal area), D the size of nanoparticle, s the interparticle distance. The fractal dimension d_f estimated from SEM images was 1.87. It is assumed that the local concentration of gold nanoparticles is constant and the network structure grows exponentially, and N_{max} is close to the number of particles at saturation in the network structure. By this method, the minimum number of particles with distinct Raman signal at the time point, t = 3 min, was approximately estimated as 14, for a network size of 163 nm.

Below, we demonstrate the feasibility of detecting two cell surface markers using two Raman tags to, respectively, detect CD44 and CD24 receptors. The proof-of-concept cell surface receptor detection strategy with single target detection sensitivity was first illustrated through a simple antigen−antibody interaction study (details are provided in the Supporting Information section SI.3). Raman mapping of two different nonfluorescent labels, 4-mercaptopyridine (characteristic peak at 1094 cm^{-1}) and 4,6-dimethyl-2-pyrimidinethiol (characteristic peak at 569 cm^{-1}) representing CD44 and CD24, respectively, was conducted to assess the distribution of these surface markers on selected cancer cells. MCF-7, MDA-MB-231, and MDA-MB-468 show the respective expression of CD24, CD44, and CD44/CD24 in Figure 3b (i−iii). The SERS signal corresponding to CD44 disappeared (melting point of the network structure was ∼35 °C) from MDA-MB-468 cells subjected to a water bath temperature of 35 °C for 15 min. However, the signal from the Raman label, depicting the CD24 marker, persisted (Figure 3b (iv)) because the melting point of the hybridized structures to denote CD24 was 45 °C. However, when the temperature was increased to 45 °C, both the signals disappeared, indicating that the structure has disintegrated (Figure 3b (v)).

The dynamic change in the SERS intensity (at 1094 cm^{-1}) of the Raman dye, 4-mercaptopyridine, functionalized on the enhancer particle with respect to time during network structure formation is shown in Figure 3c.[30] The consistent increase in Raman signal from the network structure could be attributed to the enhancement factor (in the range from ∼10^3 to ∼10^7), from the dye-embedded network assembly.[30] However, this enhancement is not observed in the controls, which consisted of cells only or cells with the nanoparticle structure without Raman dyes (Supporting Information, section SI.6). In these experiments, the concentration of the pointer and enhancer particles was ∼450 pM. This short-time growing feature of the structure on the living cell membrane is attractive because it eliminates cellular uptake of targeted nanoparticles and provides the possibility of detecting several biomarkers at single cell resolution. It is also worth noting that, since the enhancement from the nanoparticle network structure is strong enough, Raman measurement was possible even with a very low laser power (1 mW) and a short integration time (3∼30 s), virtually avoiding cell damage, making this an ideal platform for intracellular and *in vivo* studies.

It should be noted that the size of the network and the time of network formation can be controlled by the concentration of enhancer particles (Figure 3c). We illustrate this by using a concentration of ∼70 pM (∼7-fold dilution of the original concentration of 450 pM). It should be noted that the aggregation kinetics is primarily controlled by the particle concentration described in eq 1, while factors such as nanoparticle size, temperature, and the number of DNA on nanoparticles are fixed as described in sample preparation (Figure 1). Experiments indicated that it took ∼18 min to produce

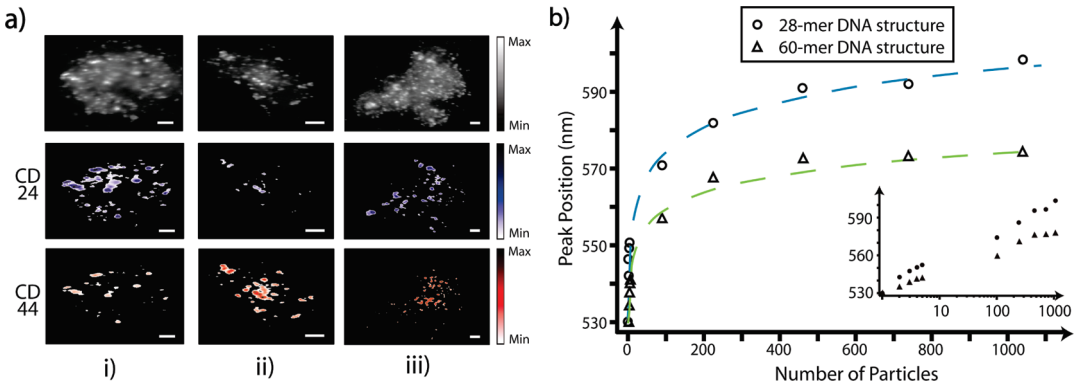

Figure 4. (a) Dark-field images of gold nanoparticle network structures on three different cell lines based on intensities at all wavelengths (top), 604 nm (middle, pseudo-blue), and 578 nm (bottom, pseudo-red); (i) MCF-7, (ii) MDA-MB-231, and (iii) MDA-MB-468. Images in (i) and (ii) show the distribution of short (CD24) or long wavelength (CD44) of LSPRS peak only; (iii) shows the short and long wavelength (scale bar = 10 μm). (b) Plasmon resonance peak positions according to the number of nanoparticles in a network. Dark-field spectroscopy measurements (except for 3−5 nanoparticles, which are from FDTD simulation results) are fitted by the suggested equation $\Delta\lambda/\lambda_0 = 0.41 \times \log(N) \times \exp(-6.91 \times s/D)$.

a signal of comparable intensity to that obtained with the initial concentration of 450 pM in 3.5 min (Figure 3c). The comparable intensities imply a similar size of the network structure. Our experiments indicate that, at lower concentrations of the enhancer particles, consistent SERS signal in proportion to the network size was possible. However, when the particle concentration is kept too low (less than 30 pM), the rate of cellular uptake could dominate, preventing any aggregate formation. During the first few minutes, an increase in signal intensity, denoting enhancement due to plasmon coupling, was possible as noted by the exponential growth model (Figure 3c). A decrease in signal intensity possibly due to a decrease in particle concentration in the vicinity of the nanostructure is likely. This trend was captured in our experiments to detect CD24 and CD44 markers on cell surfaces using respective nanoparticle probes. It is common knowledge that plasmon coupling is critical for optimal enhancement. The possibility of direct measurement of the plasmon resonance suggests another important measurement method, the hyperspectral localized SPR in scattering (LSPRS).[37,38]

Hyperspectral LSPRS has its pros and cons. An advantage of this method is its high resolution compared to normal optical microscopy because of the use of a slit or pinhole, promising spatial localization at a high resolution. Hyperspectral LSPR is faster, better in resolution, and, more importantly, it does not require any labeling of the molecule, which makes the synthesis and measurement process more versatile and robust compared to SERS. Hyperspectral LSPRS imaging has been used in targeted drug delivery, tumor cell differentiation, and quantification.[39] Multiplex detection, using nanomaterials fabricated from gold,[40] silver,[41] fluorescent probes,[42] and quantum dots,[43] has also been attempted. While imaging/detection in general is based on intensity, LSPRS examines the peak shift of two different gold nanoparticle network structures with different interspacing due to the use of 28 and 60 base pair hybridizations that yield a significant shift in the peak of the plasmon band by as much as 26 nm (Figure 4b). Interparticle distance-dependent diagnostics is yet another useful multiplexing metric and can be successfully harnessed by highly resolved hyperspectral imaging. Hyperspectral images, namely, SERS and LSPRS mapping, confirm the reliability of the gold nanoparticle network structure not only for SERS but also for plasmon-based detection of CD44/CD24 markers in the cell lines tested using appropriate networks.

Hyperspectral LSPRS images of plasmon probes (functionalized gold nanoparticles) targeting CD44 and CD24 markers from the three cell lines are presented in Figure 4 to complement and confirm the results obtained by Raman mapping (Figure 3 (i−v)). As a negative control, MDA-MB-468 cells were tested in two types of experiments. First, the cells were incubated with gold nanoparticles modified only with DNA (using enhancer particles only) showing no clear binding phenomena, with the exception of a possible nonspecific binding (Supporting Information Figure S4c). Second, if the cells were incubated with only pointer particles (*i.e.*, gold nanoparticles modified with antibodies and ssDNA), a distinct peak around 530 nm (from single nanoparticles) could be detected, confirming the absence of the network structure (Supporting Information Figure S4d). From the results of SPR imaging in Figure 4a (i), MCF-7 shows the predominance of CD24 expression with low expression of CD44. Figure 4a (ii) shows the distribution of CD44 in MDA-MB-231, and Figure 4a (iii) reveals the presence of both the CD44 and CD24 markers in MDA-MB-468 cells. Immunophenotying of the cell population, studied by counting the number of each immunotype (CD44+/CD24+, CD44+/CD24−, CD44+/CD24−, CD44+/CD24−) detected by LSPRS peaks at 604 and 578 nm corresponding to the plasmon response

TABLE 1. Comparison of Results from Hyperspectral Imaging (LSPRS) and Conventional Cytometry Sorting (Data from Reference 2)

	MCF7		MDA-MB-231		MDA-MB-468	
	this work	cytometry	this work	cytometry	this work	cytometry
CD24+/CD44+	14.3	8 ± 3	3.6	2	85.7	90 ± 6
CD24−/CD44+	0	0	85.7	85 ± 5	7.2	3 ± 1
CD24+/CD44	82.2	87 ± 3	0	0	7.1	7 ± 3
CD24/CD44	3.5	6 ± 1	10.7	13 ± 5	0	0

of the network structure, shows excellent agreement with cytometry results from the literature (Table 1).[2,44]

Clear differentiation of two different structures by hyperspectral LSPRS suggests an obvious functional feature of the gold nanoparticle network structure, namely, wavelength specificity, which can be harnessed to impart photothermal effect when excited at that resonance.[45,46] When the nanoparticle structure is excited at its resonance wavelength, it behaves as an efficient light absorber, resulting in the conversion of the optical energy to thermal energy.[47,48] When the gold nanoparticle network structures are excited by a laser of wavelength 633 or 568 nm, the structures with a resonance at ~604 or ~578 nm produced by the nanoparticle assembly are disassembled (Supporting Information section SI.7).

The versatility of the formed structures to impart selective heating effect at a localized region of the assembly is especially encouraging because treatment can be administered to a specific biomarker site leaving the rest of the system intact due to spectral selectivity. A clear separation of the plasmon resonance peak could be obtained by controlling the sequence length, the number of DNA molecules on the nanoparticle surface, and the size of nanoparticles. The number of particles in the network structure can be controlled by the density of complementary molecules (ssDNA). When the number of DNA molecules on the nanoparticle surface is high or if the length of the sequence is long, the longer is the hybridization time.[49,50] Such localized heating strategies using plasmon structures can be designed to promote gene release[51] and highly specific tumor cell ablation platforms.[52]

It is practically important to extrapolate that the plasmon resonance peak shifts with a relatively simple formula. Dependence of the number of nanoparticles in the network can be described in logarithmic terms based on their fractal formation.[53] Indeed, Wang *et al.* measured a peak shift of about 170 nm in their sub-10-nm gap nanoparticle array,[54] while a dimer structure with the same interparticle distance shows a shift of ~40[55] and 80 nm[56] when they are separated by a distance of 1 nm. The peak shift from the gold nanoparticle network can thus be written in a generalized form as

$$\Delta\lambda/\lambda_0 = A \times \log(q \times N + r) \times \exp(-Bs/D) \quad (2)$$

where $A = 0.41 \pm 0.057$, $B = 6.92 \pm 0.263$, $q = 1$, $r \sim 0$. Coefficients A and B are obtained from fitting for the functions in the region of a large number of particles (Figure 4b), and coefficients p and q are obtained from the experimental data of dimers/trimers and FDTD simulation results (Supporting Information section SI.2) based on the assumption that, when the number of nanoparticles are very small (2−3 particles), particles can form a linear structure with very high probability. The models (eq 2) developed in this work are also applicable to characterize structures formed by two or three particles studied by others.[55,57−59]

In conclusion, we demonstrate a reversible network structure with application in diagnostics at single cell resolution. This gold nanoparticle network is grown using DNA hybridization on the cell surface marker sites and provides an efficient platform for detection with SERS and localized SPR in scattering to achieve multiplexing (CD44 and CD24) at a very high resolution in three different types of cancer cells. The hyperspectral SPR and images using SERS tags show excellent agreement, good control, and stability, confirming the complementary advantages of the dual-probe platform interrogation. The use of SERS tags for mapping provides excellent multiplexing ability, while hyperspectral SPR can be versatile, and is capable of sensing at a high spatial resolution, dynamic events such as intracellular protein assemblies. It is shown that the plasmon peak shift can be interpolated with a simple equation, and the number of particles contributing to the aggregates can be assessed. The network structure is reversible, and the signal enhancement during formation and dissipation can be dynamically monitored on cell surfaces in a multiplex format. Multifunctional gold nanoparticle networks are attractive because their unique properties can enable a variety of detection modalities for biomedical applications.

EXPERIMENTAL SECTION

Forty nanometer seed gold nanoparticles were synthesized by citrate reduction of $HAuCl_4$.[60,61] One micromolar of ssDNA (short sequence: 5′-AAA AAA AAG AAT TGG CTG CT-3′, and 5′-AAA AAA AAA GCA GCC AAT TC-3′, long sequence (sandwich): 5′-GCT GCT TGT GAA TTT TCT GAT TTT TTT TTT-3′, 5′-TCA GAA AAT TCA CAA GCA GCC AAT TCA ATG LABEL ACA GAC G-3′, and 5′-TTT TTT TTT TCG TCT GTC TAC ATT GAA TTG-3′) and Raman tags were fabricated to constitute enhancer particles by the methods introduced in our earlier efforts.[62,63] Pointer particles were modified with antibody and ssDNA by a method introduced by Hill *et al.*[64](Supporting Information section SI.4).

Samples were obtained at 0, 5, 20, and 40 min incubation times and washed with deionized distilled water (>18.2 MΩ) four times and dried for FESEM (field emission scanning electron microscopy) imaging and Raman mapping. Different samples of MDA-MB-468 were prepared to illustrate the reversibility of the network structure formation. Enhancer particles in the network structures were removed by DNA dehybridization by a temperature step. For short sequence (28 bps) structures, the melting temperature was 35 °C, and for long sequence (60 bps) structures, the melting temperature was 45 °C, with an exposure time of 15 min in 0.15× PBS buffer (Supporting Information section SI.5). All measurements were performed in PBS buffer and replicated three times.

Breast cancer cell lines, MCF-7, were grown in DMEM (10% fetalplex, 5% CO_2, 37 °C), and both MDA-MB-231 and MDA-MB-468 were grown in RPMI1630 (10% fetalplex, 5% CO_2, 37 °C). All cells were cultured in 18 mm round coverslips in a 6-well plate and fixed when the cells reached about 80% confluence. For fixation, cells were incubated with 4% paraformaldehyde for 20 min and rinsed with PBS, then dried. For cell surface marker detection, pointer particles, modified with antibodies and ssDNA, anti-CD44-long sequence DNA, and anti-CD24-short sequence DNA, respectively, were fabricated to first target and bind to the cell surface with a 15−20 min incubation to allow its binding to the respective cell surface markers (CD44, CD24). The samples were washed twice with PBS buffer, and enhancer nanoparticles were added to form gold nanoparticle structures by hybridization. After 30 min of incubation in PBS, the sample was washed and diluted in PBS buffer (0.15× PBS) to remove unbound nanoparticles. SERS signal was measured by Raman spectroscopy (Nicolet Almega XR dispersive Raman spectrometer, Thermo Scientific, Waltham, MA) with a 785 nm laser excitation and 1 mW power using an acquisition time of 3 s. All measurements were done with a 50× objective (NA = 0.75, infinity and flat corrected). Mapping corresponding to the key peaks of the Raman label used for cell marker detection shows the distribution of the network structure and the identity of cell surface markers located at the same position. Raman peaks at 1094 and 569 cm^{-1} were mapped to represent 4-mercaptopyridine and 4,6-dimethyl-2-pyrimidinethiol, respectively.

Acknowledgment. Funding for this work is provided by the Trask grant from Purdue University and the NSF-IDBR-0754740 grant (Co−PI) to J.I.

Supporting Information Available: Details on the network structure, FDTD simulation and experimental results of plasmon resonance peak shift, *in vitro* experiments of structure formation, melting point study, control images of SERS and dark-field hyperspectral images, and photothermal disassembly of gold nanoparticle network structures (*in vitro*) are presented. This material is available free of charge *via* the Internet at http://pubs.acs.org.

REFERENCES AND NOTES

1. Al-Hajj, M.; Wicha, M. S.; Benito-Hernandez, A.; Morrison, S. J.; Clarke, M. F. Prospective Identification of Tumorigenic Breast Cancer Cells. *Proc. Natl. Acad. Sci. U.S.A.* **2003,** *100*, 3983–3988.
2. Sheridan, C.; Kishimoto, H.; Fuchs, R. K.; Mehrotra, S.; Bhat-Nakshatri, P.; Turner, C. H.; Goulet, R.; Badve, S.; Nakshatri, H. CD44+/CD24− Breast Cancer Cells Exhibit Enhanced Invasive Properties: An Early Step Necessary for Metastasis. *Breast Cancer Res.* **2006,** *8*, R59.
3. Croker, A. K.; Goodale, D.; Chu, J.; Postenka, C.; Hedley, B. D.; Hess, D. A.; Allan, A. L. High Aldehyde Dehydrogenase and Expression of Cancer Stem Cell Markers Selects for Breast Cancer Cells with Enhanced Malignant and Metastatic Ability. *J. Cell. Mol. Med.* **2008,** *13*, 2236–2252.
4. Iida, N.; Bourguignon, L. Y. W. New CD44 Splice Variants Associated with Human Breast Cancers. *J. Cell. Physiol.* **1995,** *162*, 127–133.
5. Bruchez, M., Jr.; Moronne, M.; Gin, P.; Weiss, S.; Alivisatos, A. P. Semiconductor Nanocrystals as Fluorescent Biological Labels. *Science* **1998,** *281*, 2013–2016.
6. Yezhelyev, M. V.; Al-Hajj, A.; Morris, C.; Marcus, A. I.; Liu, T.; Lewis, M.; Cohen, C.; Zrazhevskiy, P.; Simons, J. W.; Rogatko, A.; *et al. In Situ* Molecular Profiling of Breast Cancer Biomarkers with Multicolor Quantum Dots. *Adv. Mater.* **2007,** *19*, 3146–3151.
7. Wang, C.; Chen, J.; Talavage, T.; Irudayaraj, J. Gold Nanorod/Fe_3O_4 Nanoparticle "Nano-Pearl-Necklaces" for Simultaneous Targeting, Dual-Mode Imaging, and Photothermal Ablation of Cancer Cells. *Angew. Chem., Int. Ed.* **2009,** *48*, 2759–2763.
8. Yu, C.; Nakshatri, H.; Irudayaraj, J. Identity Profiling of Cell Surface Markers by Multiplex Gold Nanorod Probes. *Nano Lett.* **2007,** *7*, 2300–2306.
9. Choi, Y.; Kang, T.; Lee, L. P. Plasmon Resonance Energy Transfer (PRET)-Based Molecular Imaging of Cytochrome *c* in Living Cells. *Nano Lett.* **2008,** *9*, 85–90.
10. Schlucker, S.; Schluecker, S.; Kustner, B.; Punge, A.; Bonfig, R.; Marx, A.; Strobel, P. Immuno-Raman Microspectroscopy: *In Situ* Detection of Antigens in Tissue Specimens by Surface-Enhanced Raman Scattering. *J. Raman Spectrosc.* **2006,** *37*, 719–721.
11. Wu, L. Y.; Ross, B. M.; Hong, S.; Lee, L. P. Bioinspired Nanocorals with Decoupled Cellular Targeting and Sensing Functionality. *Small* **2010,** *6*, 503–507.
12. Huang, X.; El-Sayed, I. H.; Qian, W.; El-Sayed, M. A. Cancer Cells Assemble and Align Gold Nanorods Conjugated to Antibodies To Produce Highly Enhanced, Sharp, and Polarized Surface Raman Spectra: A Potential Cancer Diagnostic Marker. *Nano Lett.* **2007,** *7*, 1591–1597.
13. El-Sayed, I. H.; Huang, X.; El-Sayed, M. A. Surface Plasmon Resonance Scattering and Absorption of Anti-EGFR Antibody Conjugated Gold Nanoparticles in Cancer Diagnostics: Applications in Oral Cancer. *Nano Lett.* **2005,** *5*, 829–834.
14. Huang, M. J.; Ling, M.; Zhi, G.; Qian, Y.; Dai, M.; Yi, X.; Mei, L.; Ke, C.; Jian, W.; Jing, Z.; *et al.* One-Step Preparation of Poly(ε-caprolactone)−Poly(ethylene glycol)−Poly(ε-caprolactone) Nanoparticles for Plasmid DNA Delivery. *J. Biomed. Mater. Res., Part A* **2008,** *86A*, 979–986.
15. Chen, J.; Jiang, J.; Gao, X.; Gong, J.; Shen, G.; Yu, R. Gold-Aggregated, Dye-Embedded, Polymer-protected Nanoparticles (GDPNs): A New Type of Tags for Detection with SERS. *Colloids Surf., A* **2007,** *294*, 80–85.
16. McCabe, A. F.; Eliasson, C.; Prasath, R. A.; Hernandez-Santana, A.; Stevenson, L.; Apple, I.; Cormack, P. A. G.; Graham, D.; Smith, W. E.; Corish, P.; *et al.* SERRS Labelled Beads for Multiplex Detection. *Faraday Discuss.* **2006,** *132*, 303–308.
17. Jiang, Y.; Horimoto, N. N.; Imura, K.; Okamoto, H.; Matsui, K.; Shigemoto, R. Bioimaging with Two-Photon-Induced Luminescence from Triangular Nanoplates and Nanoparticle Aggregates of Gold. *Adv. Mater.* **2009,** *21*, 2309–2313.
18. Su, X.; Zhang, J.; Sun, L.; Koo, T.-W.; Chan, S.; Sundararajan, N.; Yamakawa, M.; Berlin, A. A. Composite Organic−Inorganic Nanoparticles (COINs) with Chemically Encoded Optical Signatures. *Nano Lett.* **2005,** *5*, 49–54.
19. Huang, P.-J.; Chau, L.-K.; Yang, T.-S.; Tay, L.-L.; Lin, T.-T. Nanoaggregate-Embedded Beads as Novel Raman Labels for Biodetection. *Adv. Funct. Mater.* **2009,** *19*, 242–248.
20. Mulvaney, S. P.; Musick, M. D.; Keating, C. D.; Natan, M. J. Glass-Coated, Analyte-Tagged Nanoparticles; A New Tagging System Based on Detection with Surface-Enhanced Raman Scattering. *Langmuir* **2003,** *19*, 4784–4790.
21. Kustner, B.; Gellner, M.; Schutz, M.; Schoppler, F.; Marx, A.; Strobel, P.; Adam, P.; Schmuck, C.; Schlucker, S. SERS Labels for Red Laser Excitation: Silica-Encapsulated SAMs on Tunable Gold/Silver Nanoshells. *Angew. Chem., Int. Ed.* **2009,** *48*, 1950–1953.
22. Schwartzberg, A. M.; Grant, C. D.; Wolcott, A.; Talley, C. E.; Huser, T. R.; Bogomolni, R.; Zhang, J. Z. Unique Gold Nanoparticle Aggregates as a Highly Active Surface-Enhanced Raman Scattering Substrate. *J. Phys. Chem. B* **2004,** *108*, 19191–19197.
23. Kneipp, K.; Kneipp, H.; Manoharan, R.; Hanlon, E. B.; Itzkan, I.; Dasari, R. R.; Feld, M. S. Extremely Large Enhancement

Factors in Surface-Enhanced Raman Scattering for Molecules on Colloidal Gold Clusters. *Appl. Spectrosc.* **1998,** *52*, 1493–1497.
24. Brown, L. O.; Doorn, S. K. Optimization of the Preparation of Glass-Coated, Dye-Tagged Metal Nanoparticles as SERS Substrates. *Langmuir* **2008,** *24*, 2178–2185.
25. Mirkin, C. A.; Letsinger, R. L.; Mucic, R. C.; Storhoff, J. J. A DNA-Based Method for Rationally Assembling Nanoparticles into Macroscopic Materials. *Nature* **1996,** *382*, 607–609.
26. Alivisatos, A. P.; Johnsson, K. P.; Peng, X.; Wilson, T. E.; Loweth, C. J.; Bruchez, M. P.; Schultz, P. G. Organization of Nanocrystal Molecules Using DNA. *Nature* **1996,** *382*, 609–611.
27. Elghanian, R.; Storhoff, J. J.; Mucic, R. C.; Letsinger, R. L.; Mirkin, C. A. Selective Colorimetric Detection of Polynucleotides Based on the Distance-Dependent Optical Properties of Gold Nanoparticles. *Science* **1997,** *277*, 1078–1081.
28. Graham, D.; Thompson, D. G.; Smith, W. E.; Faulds, K. Control of Enhanced Raman Scattering Using a DNA-Based Assembly Process of Dye-Coded Nanoparticles. *Nat. Nanotechnol.* **2008,** *3*, 548–551.
29. Bao-An, D.; Zheng-Ping, L.; Cheng-Hui, L. One-Step Homogeneous Detection of DNA Hybridization with Gold Nanoparticle Probes by Using a Linear Light-Scattering Technique. *Angew. Chem., Int. Ed.* **2006,** *45*, 8022–8025.
30. Lee, K.; Irudayaraj, J. Periodic and Dynamic 3-D Gold Nanoparticle−DNA Network Structures for Surface-Enhanced Raman Spectroscopy-Based Quantification. *J. Phys. Chem. C* **2009,** *113*, 5980–5983.
31. Robert, J. S.; Alexandra, M.; Lundahl, P. J.; Smith, W. E.; Karen, F.; Duncan, G. Quantitative Enhanced Raman Scattering of Labeled DNA from Gold and Silver Nanoparticles. *Small* **2007,** *3*, 1593–1601.
32. Zou, S.; Janel, N.; Schatz, G. C. Silver Nanoparticle Array Structures That Produce Remarkably Narrow Plasmon Lineshapes. *J. Chem. Phys.* **2004,** *120*, 10871–10875.
33. Genov, D. A.; Sarychev, A. K.; Shalaev, V. M.; Wei, A. Resonant Field Enhancements from Metal Nanoparticle Arrays. *Nano Lett.* **2004,** *4*, 153–158.
34. Chithrani, B. D.; Chan, W. C. W. Elucidating the Mechanism of Cellular Uptake and Removal of Protein-Coated Gold Nanoparticles of Different Sizes and Shapes. *Nano Lett.* **2007,** *7*, 1542–1550.
35. Ellen, E. C.; Judith, M.; Anand, G.; Catherine, J. M.; Michael, D. W. Gold Nanoparticles Are Taken up by Human Cells but Do Not Cause Acute Cytotoxicity. *Small* **2005,** *1*, 325–327.
36. Park, S. Y.; Stroud, D. Structure Formation, Melting, and Optical Properties of Gold/DNA Nanocomposites: Effects of Relaxation Time. *Phys. Rev. B* **2003,** *68*, 224201.
37. Jensen, T. R.; Malinsky, M. D.; Haynes, C. L.; Van Duyne, R. P. Nanosphere Lithography: Tunable Localized Surface Plasmon Resonance Spectra of Silver Nanoparticles. *J. Phys. Chem. B* **2000,** *104*, 10549–10556.
38. Haes, A. J.; Zou, S.; Schatz, G. C.; VanDuyne, R. P. Nanoscale Optical Biosensor: Short Range Distance Dependence of the Localized Surface Plasmon Resonance of Noble Metal Nanoparticles. *J. Phys. Chem. B* **2004,** *108*, 6961–6968.
39. Beach, J. Hyperspectral Microscopy Combines Disparate Methodologies To Produce a Data-Rich View of Biological Structures Useful in Research and Clinical Applications. *Biooptics World* **2009,** 2.
40. Aaron, J.; de la Rosa, E.; Travis, K.; Harrison, N.; Burt, J.; José-Yacamán, M.; Sokolov, K. Polarization Microscopy with Stellated Gold Nanoparticles for Robust Monitoring of Molecular Assemblies and Single Biomolecules. *Opt. Express* **2008,** *16*, 2153–2167.
41. Vo-Dinh, T.; Yan, F.; Wabuyele, M. B. Surface-Enhanced Raman Scattering for Medical Diagnostics and Biological Imaging. *J. Raman Spectrosc.* **2005,** *36*, 640–647.
42. Alluri, P. G.; Reddy, M. M.; Bachhawat-Sikder, K.; Olivos, H. J.; Kodadek, T. Isolation of Protein Ligands from Large Peptoid Libraries. *J. Am. Chem. Soc.* **2003,** *125*, 13995–14004.
43. Yang, J.; Dave, S. R.; Gao, X. Quantum Dot Nanobarcodes: Epitaxial Assembly of Nanoparticle−Polymer Complexes in Homogeneous Solution. *J. Am. Chem. Soc.* **2008,** *130*, 5286–5292.
44. Phillips, T. M.; McBride, W. H.; Pajonk, F. The Response of CD24−/low/CD44+ Breast Cancer-Initiating Cells to Radiation. *J. Natl. Cancer Inst.* **2006,** *98*, 1777–1785.
45. Stehr, J.; Hrelescu, C.; Sperling, R. A.; Raschke, G.; Wunderlich M.; Nichtl, A.; Heindl, D.; Kurzinger, K.; Parak, W. J.; Klar, T. A.; *et al.* Gold Nanostoves for Microsecond DNA Melting Analysis. *Nano Lett.* **2008,** *8*, 619–623.
46. Maximilian, R.; Jan, C. B.; Gero von, P.; Ulrich, S. Reversible Photothermal Melting of DNA in DNA-Gold-Nanoparticle Networks. *Small* **2008,** *4*, 607–610.
47. Liu, G. L.; Kim, J.; Lu, Y.; Lee, L. P. Optofluidic Control Using Photothermal Nanoparticles. *Nat. Mater.* **2006,** *5*, 27–32.
48. Huang, X.; El-Sayed, I. H.; Qian, W.; El-Sayed, M. A. Cancer Cell Imaging and Photothermal Therapy in the Near-Infrared Region by Using Gold Nanorods. *J. Am. Chem. Soc.* **2006,** *128*, 2115–2120.
49. Storhoff, J. J.; Lazarides, A. A.; Mucic, R.; Mirkin, C.; Letsinger, R.; Schatz, G. C. What Controls the Optical Properties of DNA-Linked Gold Nanoparticle Assemblies? *J. Am. Chem. Soc.* **2000,** *122*, 4640–4650.
50. Maye, M. M.; Nykypanchuk, D.; van der Lelie, D.; Gang, O. DNA-Regulated Micro- and Nanoparticle Assembly. *Small* **2007,** *3*, 1678–1682.
51. Barhoumi, A.; Huschka, R.; Bardhan, R.; Knight, M. W.; Halas, N. J. Light-Induced Release of DNA from Plasmon-Resonant Nanoparticles: Towards Light-Controlled Gene Therapy. *Chem. Phys. Lett.* **2009,** *482*, 171–179.
52. O'Neal, D. P.; Hirsch, L. R.; Halas, N. J.; Payne, J. D.; West, J. L. Photo-thermal Tumor Ablation in Mice Using Near Infrared-Absorbing Nanoparticles. *Cancer Lett.* **2004,** *209* 171–176.
53. Park, S. Y.; Lee, J.-S.; Georganopoulou, D.; Mirkin, C. A.; Schatz, G. C. Structures of DNA-Linked Nanoparticle Aggregates. *J. Phys. Chem. B* **2006,** *110*, 12673–12681.
54. Wang, H.; Levin, C. S.; Halas, N. J. Nanosphere Arrays with Controlled Sub-10-nm Gaps as Surface-Enhanced Raman Spectroscopy Substrates. *J. Am. Chem. Soc.* **2005,** *127*, 14992–14993.
55. Reinhard, B. M.; Siu, M.; Agarwal, H.; Alivisatos, A. P.; Liphardt, J. Calibration of Dynamic Molecular Rulers Based on Plasmon Coupling between Gold Nanoparticles. *Nano Lett.* **2005,** *5*, 2246–2252.
56. Talley, C. E.; Jackson, J. B.; Oubre, C.; Grady, N. K.; Hollars, C. W.; Lane, S. M.; Huser, T. R.; Nordlander, P.; Halas, N. J. Surface-Enhanced Raman Scattering from Individual Au Nanoparticles and Nanoparticle Dimer Substrates. *Nano Lett.* **2005,** *5*, 1569–1574.
57. Jain, P. K.; Huang, W.; El-Sayed, M. A. On the Universal Scaling Behavior of the Distance Decay of Plasmon Coupling in Metal Nanoparticle Pairs: A Plasmon Ruler Equation. *Nano Lett.* **2007,** *7*, 2080–2088.
58. Maye, M. M.; Nykypanchuk, D.; Cuisinier, M.; van der Lelie, D.; Gang, O. Stepwise Surface Encoding for High-Throughput Assembly of Nanoclusters. *Nat. Mater.* **2009,** *8*, 388–391.
59. Jain, P. K.; El-Sayed, M. A. Surface Plasmon Coupling and Its Universal Size Scaling in Metal Nanostructures of Complex Geometry: Elongated Particle Pairs and Nanosphere Trimers. *J. Phys. Chem. C* **2008,** *112*, 4954–4960.
60. Frens, G. Preparation of Gold Dispersions of Varying Size: Controlled Nucleation for the Regulation of the Particle Size in Monodisperse Gold Suspensions. *Nature* **1973,** *241*, 20–22.
61. Grabar, K. C.; Freeman, R. G.; Hommer, M. B.; Natan, M. J. Preparation and Characterization of Au Colloid Monolayers. *Anal. Chem.* **1995,** *67*, 735–743.
62. Sun, L.; Yu, C.; Irudayaraj, J. Surface-Enhanced Raman Scattering Based Nonfluorescent Probe for Multiplex DNA Detection. *Anal. Chem.* **2007,** *79*, 3981–8.

63. Sun, L.; Yu, C.; Irudayaraj, J. Raman Multiplexers for Alternative Gene Splicing. *Anal. Chem.* **2008,** *80*, 3342–3349.
64. Hill, H. D.; Mirkin, C. A. The Bio-Barcode Assay for the Detection of Protein and Nucleic Acid Targets Using DTT-Induced Ligand Exchange. *Nat. Protoc.* **2006** *1*, 324–336.